



Role of cerium (Ce) dopant on structural, optical and photocatalytic properties of MgO nanoparticles by wet chemical route

V. T. Srisuvetha^{1,2,3} · S. L. Rayar^{2,3} · G. Shanthi^{1,3}

Received: 8 November 2019 / Accepted: 26 December 2019 / Published online: 8 January 2020
© Springer Science+Business Media, LLC, part of Springer Nature 2020

Abstract

Ce doped MgO nanoparticles with various doping concentrations of cerium ion were prepared by the sol–gel method. Both pure and Ce doped MgO nanoparticles were characterized by powder X-ray diffraction (XRD), Scanning electron microscope (SEM), Field emission scanning electron microscope, Energy-dispersive X-ray spectroscopy, UV–Vis diffuse reflectance spectroscopy, and Photoluminescence spectra analysis. XRD and SEM results suggest that both pristine and Ce doped MgO nanoparticles were in face centered cubic structure with individual spherical shaped nanoparticles with average particles sizes in the range of 20–30 nm. The band gap energy of pure MgO was significantly reduced from 3.81 eV to 3.22 eV. The Ce doped MgO catalyst showed outstanding photocatalytic degradation activity such as high efficiency (95%) and high stability (only loss 3.5%) towards phenol dye under visible light irradiation. The improved photocatalytic mechanism of MgO by Ce doping is also discussed.

1 Introduction

Environmental pollution has many facets, and the resultant health risks include diseases in almost all organ systems. Of particular interest is water pollution, which has become a global challenge, developing nations being highly affected due to their drive for development. The prevention of toxic chemical and biological contamination through environmentally green techniques is an important issue. In recent decades, semiconductor photocatalysis has been intensively studied for water and air treatment [1]. Generally, most of solar radiation is within the region of visible light, and hence it is significant and basic to explore photocatalysts with accessible visible light adsorption and exceedingly efficient activity [2–5]. Recently, metal oxide semiconductor materials such as TiO₂, SnO₂, WO₃, CeO₂ and ZnO have pulled in broad consideration within the recent years due to their photocatalytic capacity within the degradation of natural

pollutant in water and air. Moreover, oxide semiconductors are most reasonable candidate for broad natural applications due to their organic and chemical inactivity, solid oxidation control and cost adequacy and long-term stability against photo- and chemical corrosion [6–10].

Among the different metal oxide nanoparticles utilized for photocatalytic applications, MgO has significant interests. Magnesium oxide (MgO) is one of the foremost important functional metal oxides which have been to a great extent utilized in numerous areas such as catalysis, poisonous waste remediation, material industry, paints and superconductors [11]. Even though, the band gap (4.2 eV) and absorption of visible light is the major concern for MgO to utilize the photocatalytic activity. In addition, the performance on electron–hole separation of the MgO based photocatalyst still need to be improved. Generally, dopant is a suitable method to increase the surface area and reducing the band gap of host material, which enhance the absorption property of visible light as well as increasing the photocatalytic ability. Hence, this work we choose cerium (Ce) dopant to enhance the photocatalytic performance of bare MgO. Ce³⁺ possesses shielded 4f levels, which allow various well-defined narrow optical transitions between the spin–orbit levels and thus split the bandgap of MgO and increase the performance on electron–hole separation. One of the rare earth metal elements that commonly known as the lanthanide group

✉ V. T. Srisuvetha
srisuvetha16@gmail.com

¹ Department of Physics, Research Center Women's Christian College, Kanyakumari, Nagercoil, Tamil Nadu 629001, India

² Department of Physics, St. Jude's College, Kanyakumari, Thoothoor, Tamil Nadu 629157, India

³ Manonmaniam Sundaranar University, Abishekapatti, Tirunelveli, Tamil Nadu 627012, India

of the periodic system is cerium. Ce that showed strong absorption and emission in a visible region of UV–Vis and PL spectra. Cerium is a particular lanthanide element and it has two stable oxidation states, Ce^{3+} and Ce^{4+} (a noble gas configuration with $r = 0.90 \text{ \AA}$). Due to the high ionic radius Ce^{4+} ions are easily replaced the Mg^{2+} ions in the MgO crystal system, which enhancing the crystalline size. Owing to the increase in the size the band gap energy was also significantly reduced. Hence, we report a systematic study on the effect of Ce ion as a dopant in MgO nanoparticles. The effect of Ce doping on the electronic states, structural and optical properties and the photocatalytic activity was evaluated. The Ce dopant has positive influence in the optical and photocatalytic properties. To the best of our knowledge, this is the first report on structural, optical and photocatalytic properties of pure and Ce doped MgO nanoparticles synthesized by simple sol–gel route.

2 Experimental procedure

2.1 Materials

Cerium (IV) nitrate sulfate ($\text{CeSO}_4 \cdot 4\text{H}_2\text{O}$), Magnesium (IV) sulfate ($\text{MgSO}_4 \cdot 4\text{H}_2\text{O}$), NaOH, Congo-red and phenol solutions were purchased from Sigma-Aldrich Company with purity of 99.99%. The chemical used in the present work was analytical grade without use of any further purification.

2.2 Synthesis of pure and Ce doped MgO nanoparticles

In a typical synthesis, 2.5 g of magnesium (II) sulfate was mixed with 50 mL of ethanol under magnetic stirring to build 0.1 M solution. Then cerium (IV) sulfate was dissolved in the above solution with a molar ratio of Ce is varied from 0.00, 0.01, 0.02 to 0.05 respectively. After that NaOH solution was drop wise and again stirring with half an hour until the pH was reaches to 8.

The pH value was 6.8 before adding NaOH. Where NaOH is strong precipitate agent than KOH and NH_4OH . When NaOH is added in the precursor solution, it mixed well with the precursor solution and increased the pH of the solution as well as increased in reaction rate. Then dried at $80 \text{ }^\circ\text{C}$ at 24 h. The as prepared sample was further annealed at $500 \text{ }^\circ\text{C}$ for 3 h in air atmosphere in order to improve the crystalline nature of the samples. The pure MgO was prepared followed the similar experimental procedure without adding cerium source. The final products were named as M, CM1, CM2 and CM3 for pure, 0.01, 0.02 and 0.05% Ce doped MgO respectively.

2.3 Characterization techniques

X-ray powder diffraction (XRD) pattern of the samples were collected on a Bruker D8 Advance X-ray diffractometer using $\text{Cu K}\alpha$ radiation source (wavelength: 1.54056 \AA)

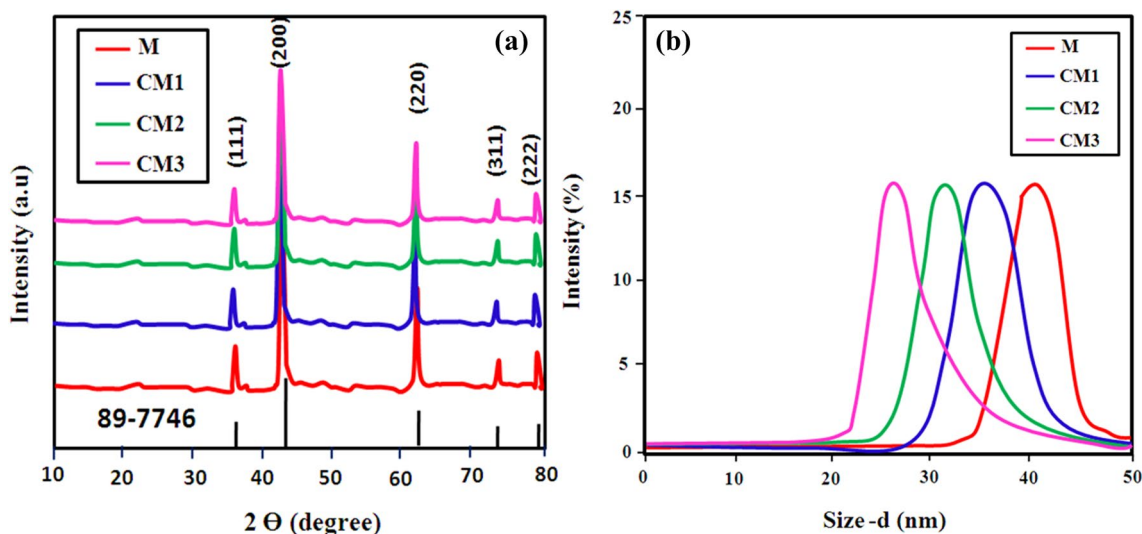


Fig. 1 a Powder XRD of pure MgO and Ce doped MgO nanoparticles, b Dynamic light scattering pattern of the samples

in the 2θ range of 10° – 80° . Transmission electron microscope (JEOL JEM 2100F Tecnai G-20, USA) operated at 200 kV, combining with Energy Dispersive X-ray spectroscopy (EDX) for the identification of morphology and elemental composition of the samples. The fundamental vibration modes of the samples were measured by using Raman spectra of the samples were recorded using BRUKER RFS 27: Stand alone FT-Raman Spectrometer at a resolution of 0.2 cm^{-1} . The specific surface areas and porous nature of materials were further investigated by nitrogen adsorption/desorption measurements on nova 2200e. The UV–Vis absorption spectrum was recorded on a Perkin–Elmer lambda 950 UV–Vis–NIR spectrophotometer.

3 Results and discussion

The X-ray diffraction patterns of undoped MgO and Ce doped MgO nanoparticles (NPs) are shown in Fig. 1a. The diffraction peaks and their relative intensities of both pure and Ce doped MgO NPs were match well with those

given by JCPDS card no. 89-7746 of MgO which indicated that all the samples had typical face centered cubic structure with space group Fm-3 m. In addition, no diffraction peaks of Ce or other impurity phases were found, hence we assume that the Ce ions have evenly substituted into the Mg^{2+} sites or interstitial sites in the MgO lattice site [12–14]. The average grain size was calculated using Scherrer's equation [15] and found to be 35, 31, 27 and 23 nm for M, CM1, CM2 and CM3 samples respectively. Malvern particle size analyzer (Model, Micro-P) was used to measure the size of nanoparticles. The average size obtained by the DLS distribution graph was around 25 to 45 nm (Fig. 1b). The dimension of both pure and doped MgO form of an equivalent sphere and sizes were found to be 40 and 25 nm for M and CM3 samples respectively. The morphology of the catalysts was analyzed via SEM and Field emission scanning electron microscope (FESEM) and the corresponding images are shown in Fig. 2. It was clear evident that both SEM and FESEM images illustrates that individual spherical shaped nanoparticles with average particles sizes in the range of 20–30 nm, which is good agreement with the XRD results. Further elemental composition of the CM3 sample was analyzed by using EDS and the related graph is shown in Fig. 2e. The sample is mainly composed of Ce, Mg and O elements. Figure 3a, b shows the N_2 adsorption–desorption isotherms and pore size distribution curve of M and CM3 samples respectively. It was clear evident that both sample showed a typical IV isotherm with a clear H_3 type hysteresis loop, which is typical characteristics of mesoporous materials [16]. The surface area and pore size was found to be $112\text{ m}^2\text{ g}^{-1}$ and 24 nm for pure MgO sample, which is higher than that of CM3 sample (surface area $62\text{ m}^2\text{ g}^{-1}$ and pore size = 37 nm). Figure 4a shows the UV-DRS analysis of all the catalyst powders. From Fig. 4a, the curve dropped sharply in a range of 325 nm then slightly shifted to 385 nm for cerium doped. In the sample of 5% Ce doped MgO, the shift is followed by an increase in the UV absorption intensity. It is well known that the absorption edge relating to band gap energy of MgO. Based on the absorption edge, the band gap energy was calculated using Kubelka–Munk (K–M) relation [17, 18] and the band gap energy was establish to be 3.81, 3.61, 3.43 and 3.22 eV for M, CM1, CM2 and CM3 samples respectively (Fig. 4b). The crystallographic information of the catalyst was further evaluated by Raman spectra and the relevant spectra are shown in Fig. 5a. The Raman spectra of bare MgO are observed for two prominent modes of 710 and 805 cm^{-1} , which is related to MgO. In Ce doped MgO, the intensity of the Raman modes are decreased and shifted to smaller wavenumber side. This may due to the size variation of both pure and Ce doped MgO samples, respectively. Figure 5b displays the room temperature PL

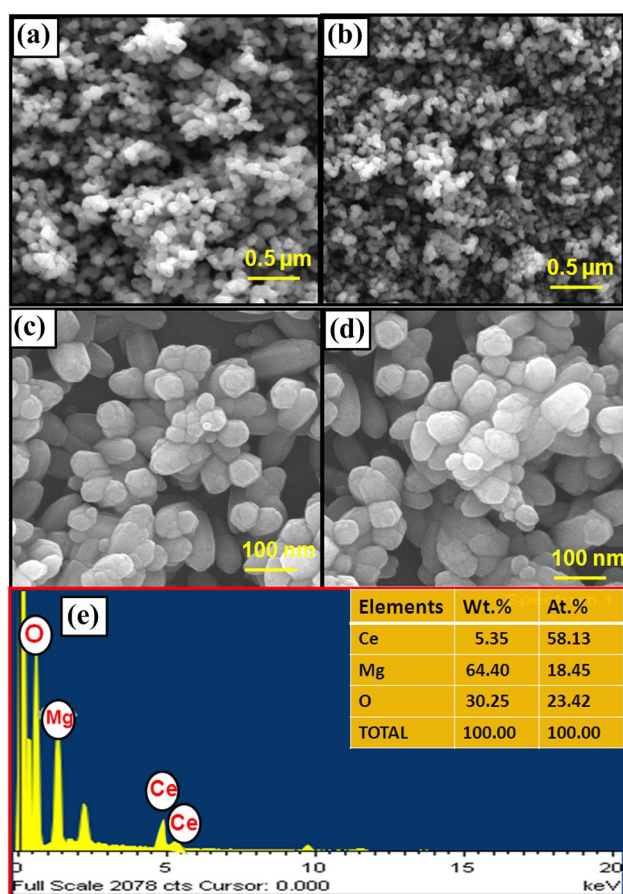


Fig. 2 SEM images of **a** M, **b** CM3, FESEM images of **c** M, **d** CM3, and **e** EDAX spectra of CM3

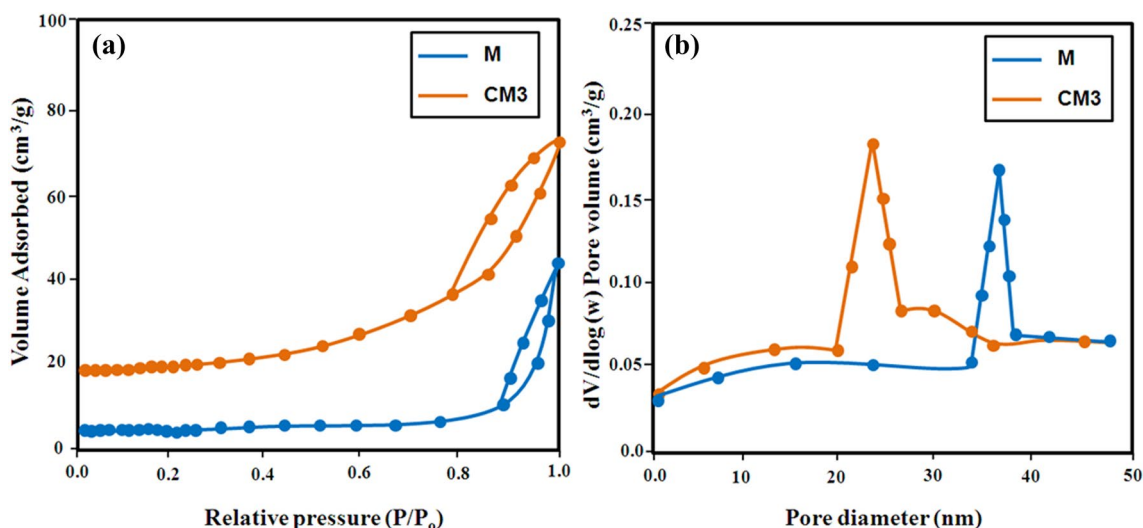


Fig. 3 a N_2 adsorption–desorption spectra, b pore size distribution of M and CM3 samples

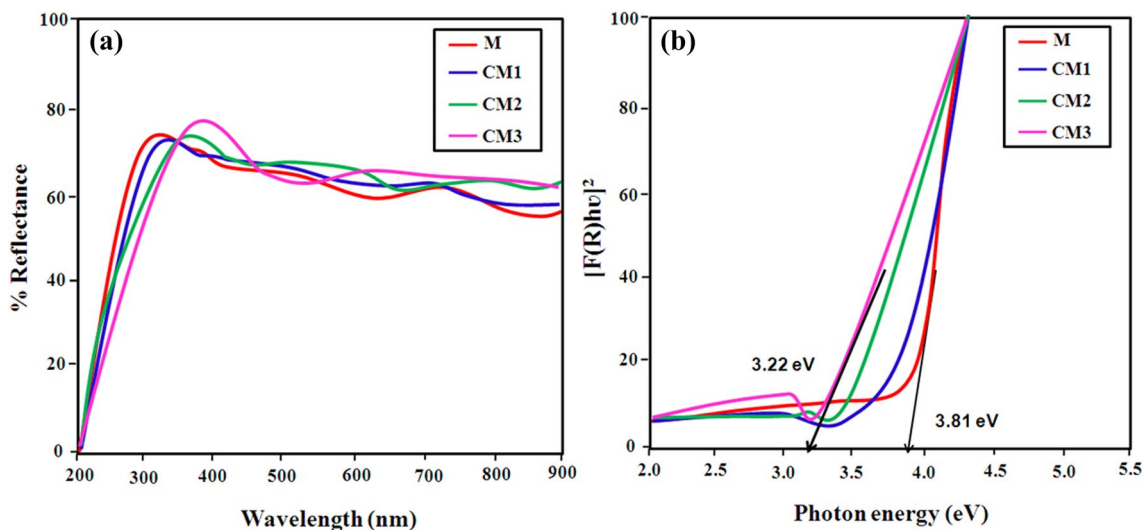


Fig. 4 UV-DRS spectra of pure MgO and Ce doped MgO nanoparticles a reflectance spectra and b K–M function

spectra of the samples with an excitation wavelength of 270 nm in the range of 200–800 nm. A broad emission band appeared around at 430 nm, which is exceptionally feasible for device applications such as UV laser innovation, scintillators and phosphors. The detailed photocatalytic set up was described below and schematic representation was shown in Fig. 6. For photocatalytic process,

the dye solution was prepared by adding a particular concentration (for example 200 mL, $C_0 = 10 \text{ mg L}^{-1}$) and a particular amount of synthesized material poured into the dye solution. In the experimental set up, 250 mL of water cooled cylindrical glass reactor with 125 W high pressure mercury lamp was used as a light source. The samples/dye solution was irradiated in the horizontal direction and the

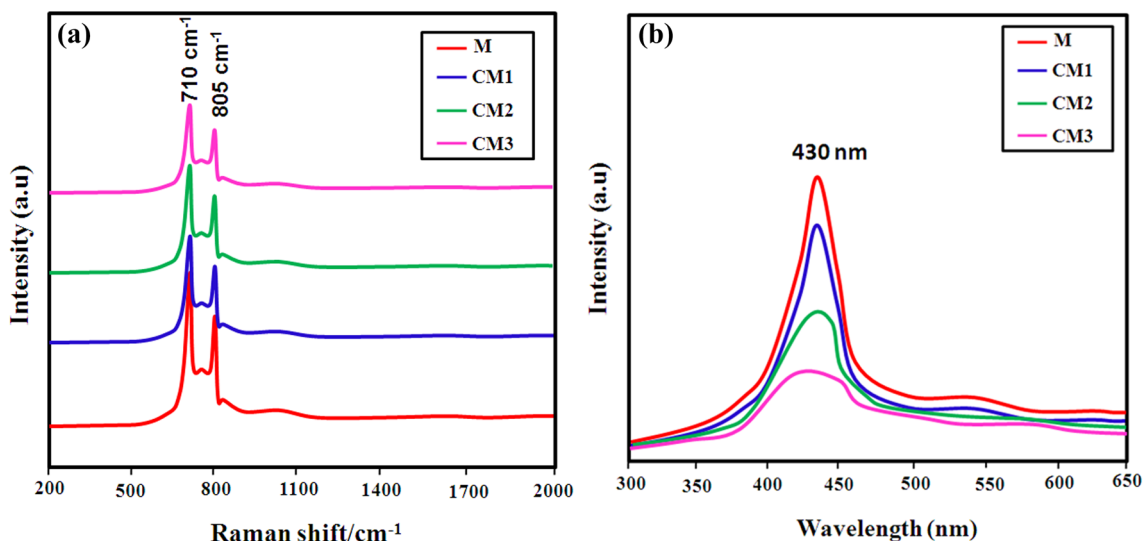


Fig. 5 **a** Raman spectra and **b** room temperature PL spectra of pure MgO and Ce doped MgO nanoparticles

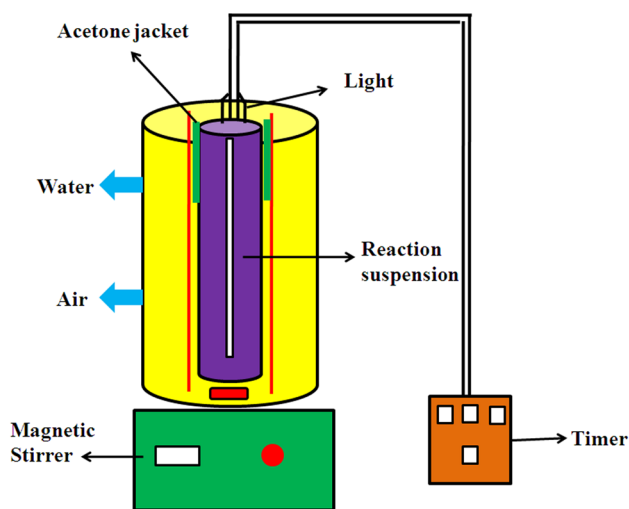


Fig. 6 Schematic representation of the photocatalytic reactor

distance between the mercury lamp and the glass/dye solution was kept within 20 cm. Then the solution was kept in the dark room and well stirred with the magnetic stirrer for more than 30 min to attain the equilibrium condition throughout the solution. The concentration of the aqueous suspensions (phenol and CR) in each sample was analyzed using UV–Vis spectrophotometer at a wavelength of 270

and 495 nm. The photocatalytic efficiency was calculated from the expression $\eta = (1 - C/C_0) \times 100$, where C_0 is the concentration of dyes (phenol and CR) before illumination and C is the concentration of dyes after a certain irradiation time. Figure 7 shows the decline of the characteristic absorption band of phenol and CR dyes using M and CM3 samples under visible light irradiation. The absorption peaks of both dyes were completely diminished after 100 min testing. After 100 min of visible light irradiation, the percentage of the photodegradation of both dyes was measured for the four samples. The result is shown in Fig. 8a, b. The maximum photocatalytic degradation efficiency was observed for CM3 and found to be 95 and 87% for phenol and CR dyes respectively. The improved photocatalytic efficiency of Ce doped MgO is due to Ce dopant promoted the transfer and separation of photogenerated electrons and holes in the bare MgO. Figure 8c, d shows the plot of $\ln(C_0/C)$ versus the irradiation time which indicates the kinetics of the reaction [19–23]. First order decay kinetics according to the following formula.

$$\ln C/C_0 = -kt$$

where C_0 is the initial concentration of dyes, C is the concentration of the dye at various interval times (mol L^{-1}), t is the illumination time (min) and k is the reaction rate constant. The rate constant (k) and the linear co-efficient

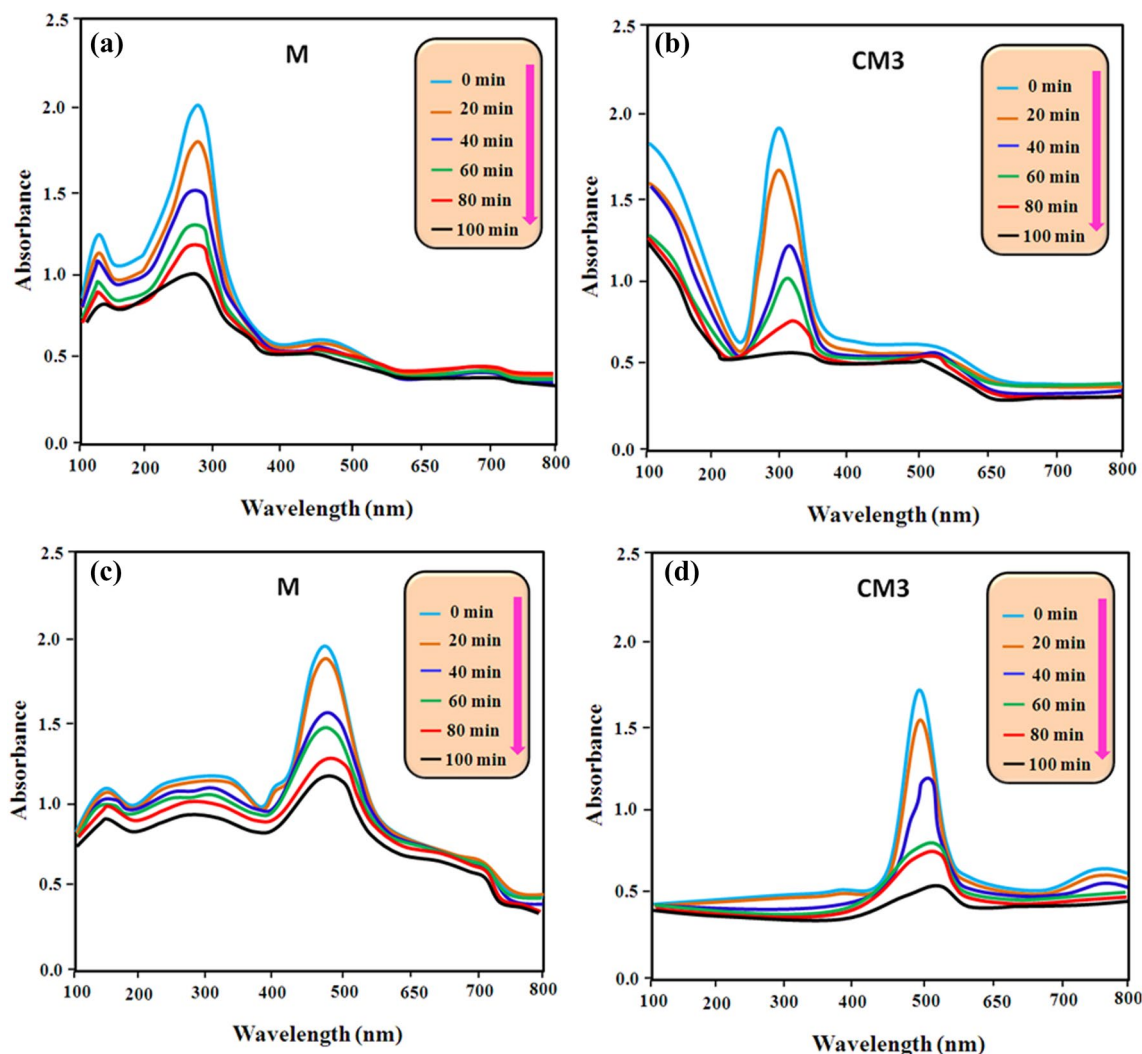


Fig. 7 The UV-light absorbance of phenol ($\lambda_{\max}=270$ nm) as a function of irradiation time (a) M and (b) CM3: absorbance spectra of CR ($\lambda_{\max}=495$ nm) as a function of irradiation time (c) M and (d) CM3

(R^2) values of CR dye were calculated to be 0.1294 min^{-1} and 0.991 respectively (CM3). Table 1 summarizes the other photocatalytic parameters of all the catalyst powders. In order to verify the high photocatalytic performance of the CM3 catalyst, different mass of (25, 50, 75 and 100 mg) the catalyst was taken and studied the photocatalytic efficiency of both dyes. The results again establish that catalyst showed outstanding photocatalytic performance (Fig. 9a, b). The stability of the catalyst is one of the important parameters to use of practical device applications. Hence, five progressive

photocatalytic tests were conducted utilizing the CM3 catalyst and by changing the dye degradation after each cycle. As can be seen in Fig. 9c, d, the photocatalytic efficiency was retain approximately 92 and 84% of its successive five cycles, which shows the great stability of Ce doped MgO catalyst. COD and TOC measurements were further carried out to estimate the toxicity of the photodegraded dye solutions and the corresponding profiles are shown in Fig. 10a, b. In phenol dye solution, it is clearly observed that COD removal (74%) and TOC removal (79%) is achieved using

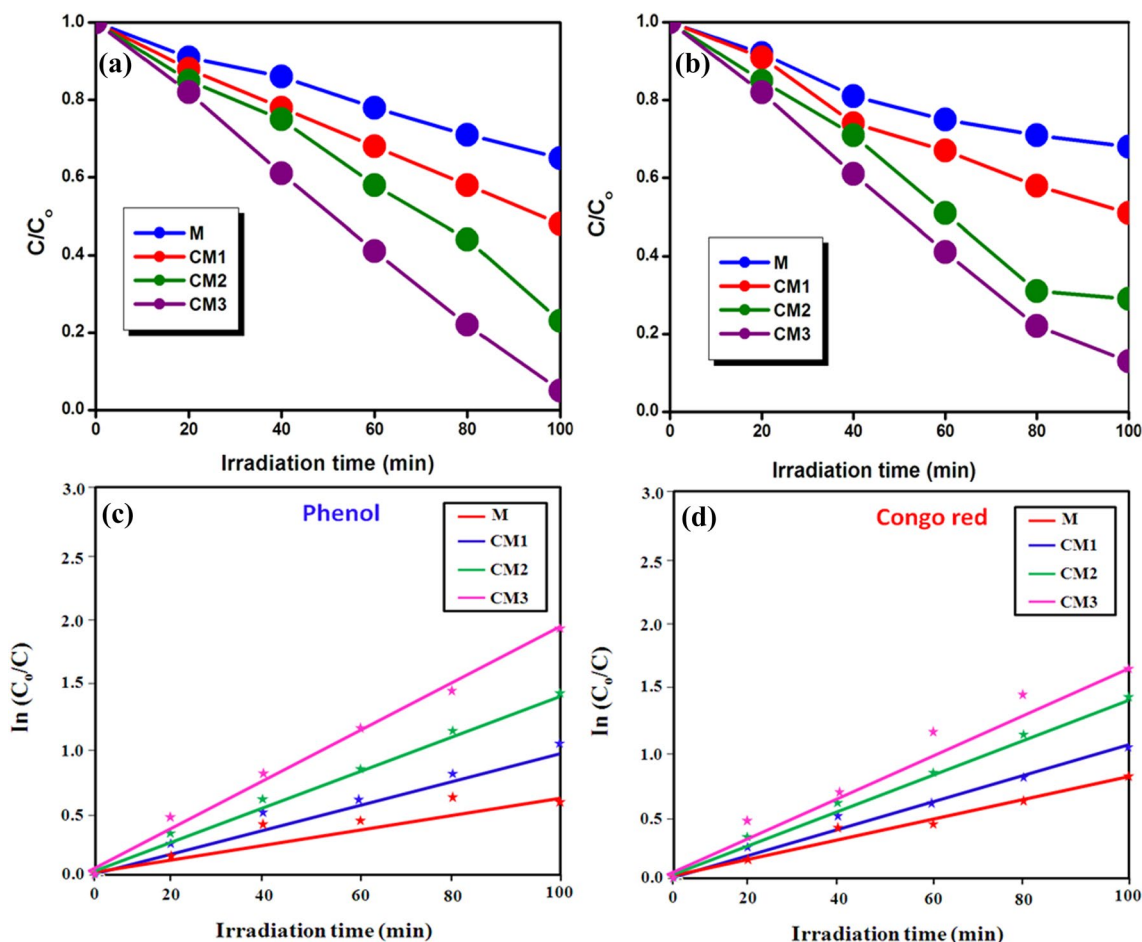


Fig. 8 **a** The temporal degradation profile of phenol and **b** degradation profile of CR (c) kinetic fit for the degradation of phenol (d) kinetic fit for the degradation of CR under visible light irradiation

Table 1 Comparison of band gap energy, rate constant and photocatalytic degradation efficiency of pure and Ce doped MgO catalyst powders

| Samples | Band gap (eV) | Rate constant of phenol | | Rate constant of CR | | Degradation efficiency at 100 min | |
|---------|---------------|-------------------------|----------------|----------------------|----------------|-----------------------------------|----|
| | | K (min ⁻¹) | R ² | K (h ⁻¹) | R ² | Phenol | CR |
| M | 3.81 | 0.0967 | 0.934 | 0.0891 | 0.921 | 35 | 32 |
| CM1 | 3.61 | 0.1001 | 0.923 | 0.0959 | 0.935 | 52 | 50 |
| CM2 | 3.43 | 0.1123 | 0.957 | 0.1098 | 0.937 | 77 | 71 |
| CM3 | 3.22 | 0.1294 | 0.991 | 0.1189 | 0.985 | 95 | 87 |

CM3 catalyst. Similarly, in CR was found to be 67% and 71% for COD and TOC respectively. Based on the photocatalytic results, the schematic representation for the present photocatalytic mechanism is shown in Fig. 10c. The overall photocatalytic results demonstrate that Ce doped MgO catalyst showed superior photocatalytic performance than pure

MgO. This could be due to the substitution of Ce³⁺ ions in the MgO crystal system, which can get oxidized to Ce⁴⁺ by discharging electrons which can encourage lead to arrangement of superoxide radicals (O₂⁻) by responding with adsorbed O₂. The oxidized Ce⁴⁺ species can act as electron scavenger or acceptor to trap photoexcited electrons from

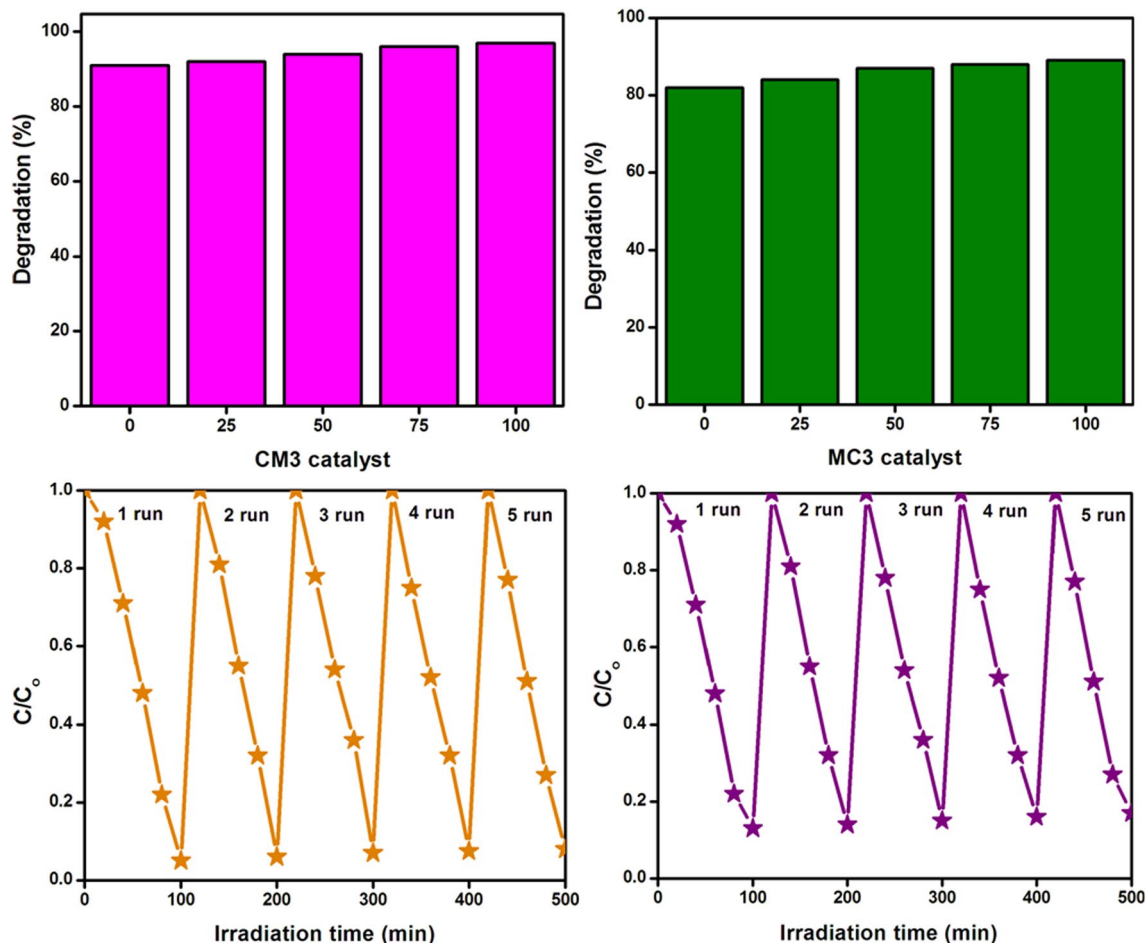


Fig. 9 a and b The effect CM3 catalyst dosage on the degradation of phenol and CR dyes respectively, c and d recycle test for the degradation of phenol and CR dyes under visible light irradiation

conduction band (CB) of MgO and subsequently reduced to Ce^{3+} . Hence, the electron (e^-)–hole (h^+) recombination can be enormously decreased driving to improved photocatalytic performance [24]. Most of the electron–hole pairs are recombined producing heat energy. However, hydroxyl radicals (HO^\bullet) are formed in the presence of electron acceptor (dissolved O_2) while hole (h^+) oxidizes water or MgO surface active ^-OH group. Dissolved O_2 reacts with the electron (e^-) and generates superoxide ion ($O_2^{\bullet-}$). Finally,

the HO^\bullet reacts with either phenol or phenolic compounds until complete mineralization. In addition, the reduction of band gap energy and gradually diminished the PL spectra intensity for the doped sample demonstrates that suppress the recombination of electron–hole pairs, which results in improving the photocatalytic performance of Ce doped MgO than pure MgO catalyst.

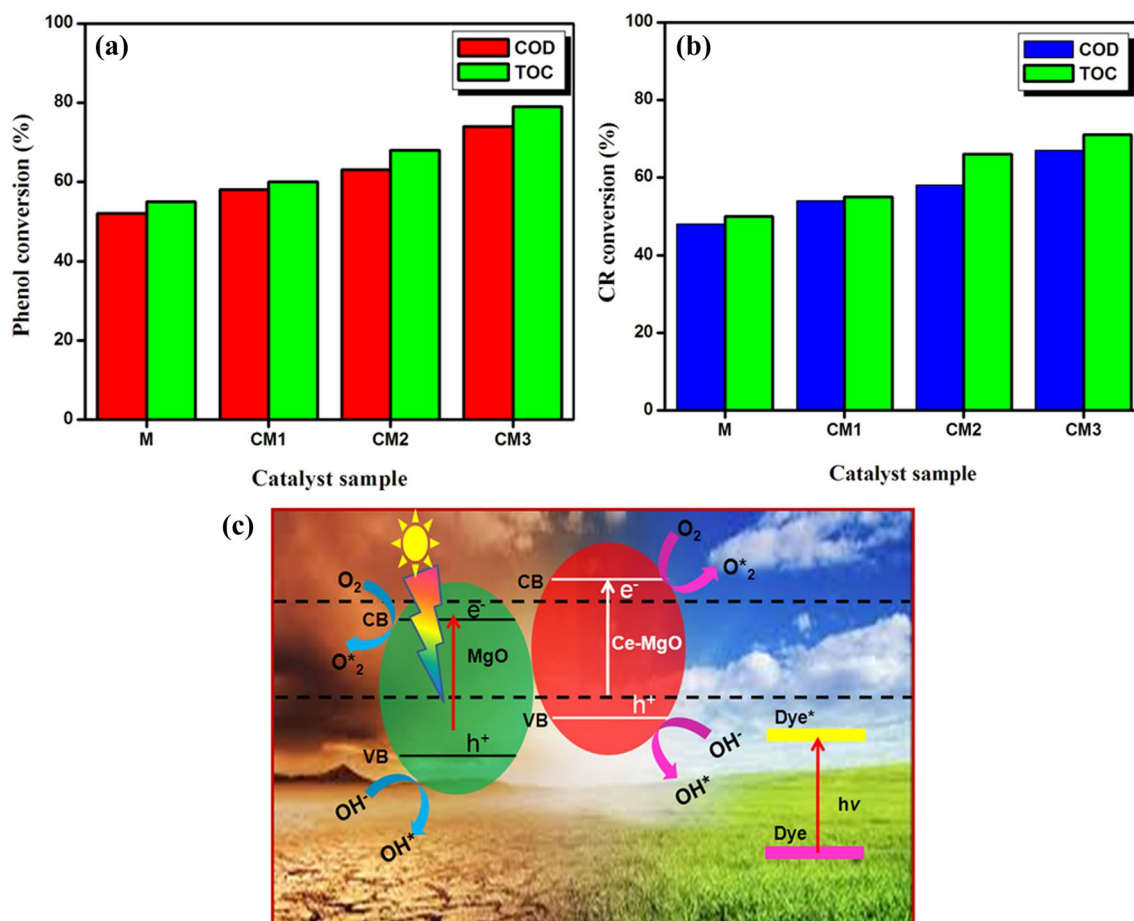


Fig. 10 **a** COD and TOC removal of phenol, **b** CR dyes using all the catalysts and **c** schematic representation for the photocatalytic mechanism of Ce doped MgO under visible light irradiation

4 Conclusions

In summary, pure and Ce doped MgO catalysts were synthesized by a facile sol–gel route and study the structural, morphological and optical properties. Powder XRD and FESEM results reveals that both pure and Ce doped MgO nanoparticles were cubic structure with spherical shaped morphology with sizes in the range of 20–30 nm. The UV and PL results exposed that absorption ability was extended to (red-shift) the visible region and reduced the recombination rate of electron–hole pairs in the Ce doped MgO catalyst. The Ce doped MgO catalyst showed outstanding photocatalytic degradation activity such as high efficiency (95%) and high stability (only loss 3.5%) towards phenol dye under visible light irradiation. The present catalysts can be preferable for highly degradation of phenol dye under visible light.

Compliance with ethical standards

Conflict of interest The authors declare that there is no conflict of interest regarding the research work reported in this manuscript.

References

1. A. Fujishima, K. Honda, *Nature* **238**, 37 (1972)
2. S. Mansingh, D.K. Padhi, K.M. Parida, *Catal. Sci. Technol.* **7**, 2772 (2017)
3. Y.C. Zhang, Z. Li, L. Zhang, L. Pan, X.W. Zhang, L. Wang, F. Aleem, J.J. Zou, *Appl. Catal. B* **224**, 101 (2018)
4. S.R. Pouran, M. Mousavi, A. HabibiYangjeh, *J. Mater. Sci. Mater. Electron.* **29**, 1719 (2018)
5. M. Pirhashemi, A. Habibi-Yangjeh, S.R. Pouran, *J. Ind. Eng. Chem.* **62**, 1 (2018)
6. O. Carp, C.L. Huisman, A. Reller, *Prog. Solid State Chem.* **32**, 33 (2004)
7. I.K. Konstantinou, T.A. Albanis, *Appl. Catal. B* **49**, 1 (2004)
8. S. Tanemura, L. Miao, W. Wunderlich, M. Tanemura, Y. Mori, S. Toh, K. Kaneko, *Sci. Technol. Adv. Mater.* **6**, 11 (2005)
9. G.K. Mor, O.K. Varghese, M. Paulose, K. Shankar, C.A. Grimes, *Sol. Energy Mater. Sol. Cells.* **90**, 2011 (2006)

10. M. Ni, M.K.H. Leung, D.Y.C. Leung, K. Sumathy, *Renew. Sustain. Energy Rev.* **11**, 401 (2007)
11. S. Suresh, D. Arivuoli, *J. Nanomater. Biostrut.* **6**, 1597 (2011)
12. V.T. Srisuvetha, S.L. Rayar, G. Shanthi, A. DhayalRaj, *Int. J. Curr. Eng. Res* **5**, 1 (2018)
13. M. Parthibavarman, M. Karthik, S. Prabhakaran, *Vacuum* **155**, 224 (2018)
14. T. Kato, G. Okada, N. Kawaguchi, T. Yanagida, *J. Lumin.* **192**, 316 (2017)
15. M. Parthibavarman, K. Vallalperuman, S. Sathishkumar, M. Durairaj, K. Thavamani, *J. Mater. Sci. Mater. Electron.* **25**, 730 (2014)
16. M. Karthik, M. Parthibavarman, A. Kumaresan, G. Prabhakaran, V. Hariharan, R. Poonguzhali, S. Sathishkumar, *J. Mater. Sci.: Mater. Electron.* **28**, 6635 (2017)
17. V. Hariharan, S. Radhakrishnan, M. Parthibavarman, R. Dhilipkumar, C. Sekar, *Talanta* **85**, 2166 (2011)
18. M. Parthibavarman, V. Hariharan, C. Sekar, V.N. Singh, *J. Optoelectron. Adv. Mater.* **12**, 1894 (2010)
19. B. Chouchene, T.B. Chaabane, L. Balan, E. Girot, K. Mozet, G. Medjahdi, R. Schneider, *Beilstein J. Nanotechnol.* **7**, 1338 (2016)
20. Y. Hao, G. Meng, C. Ye, X. Zhang, L. Zhang, *J. Phys. Chem. B.* **109**, 11204 (2005)
21. M. Parthibavarman, S. Sathishkumar, S. Prabhakaran, *J. Mater. Sci.: Mater. Electron.* **29**, 2341 (2018)
22. M. Parthibavarman, M. Karthik, S. Prabhakaran, *J. Clust. Sci.* **30**, 495 (2019)
23. M. Parthibavarman, S. Sathishkumar, M. Jayashree, R. Boopathi-Raja, *J. Clust. Sci.* **30**, 351 (2019)
24. S.P. Chaudhari, A.B. Bodade, P.D. Jolhe, S.P. Meshram, G.N. Chaudhari, *Am. J. Mater. Synth. Process.* **2**, 97 (2017)

Publisher's Note Springer Nature remains neutral with regard to jurisdictional claims in published maps and institutional affiliations.